Journal of Computational Methods in Sciences and Engineering 19 (2019) 1109–1123 1109
DOI 10.3233/JCM-193975
IOS Press

Quality evaluation of solar magnetic field images at EUV wavelengths in digital image correlation method

Yang Liu[a,b,*], Ke-Fei Song[a], Jun-Lin Ma[a], Xiao-Dong Wang[a] and Zhen-Wei Han[a]
[a]*Changchun Institute of Optics, Fine Mechanics and Physics, Chinese Academy of Sciences, Changchun, Jilin 130033, China*
[b]*University of Chinese Academy of Sciences, Beijing 100049, China*

Abstract. Application in the actual using, obviously different intensity distribution characteristics are shown in the images of solar magnetic field at extreme ultraviolet (EUV) wavelength. When it comes to displacement measurements by digital image correlation (DIC), it has a great impact on ultimate accuracy. It is an interesting and confusing issue that how to evaluate the quality of different regional solar magnetic field images at EUV wavelengths with a simple but effective parameter. This article presents a new valid part parameter for assessment of the quality of different part solar magnetic field images at EUV wavelengths used in DIC which is called comprehensive consideration of mean subset intensity and gradients (CCMSIG). Three regional images (active region, flare region, and coronal hole) are numerically translated in order to confirm that the validity of the novel concept and DIC method is used to compare the displacement measurement results with the accurate results. This paper also discusses the impact on accuracy of deformation measurements when it comes to the subset size associated with regional image quality and subset displacement functions. The results show that mean bias error and standard deviation (STD) for the sub-pixel displacement measurement are in close proximity to the CCMSIG of the calculated regional images and the high-quality regional images are supposed to be with small CCMSIG which is coincident with the theoretical predictions.

Keywords: Quality evaluation, solar magnetic field images, displacement analysis, extreme ultraviolet

1. Introduction

At present, the demand of sensor with high spatial resolution of solar magnetic field images for the research of solar physics has already reached to the order of magnitude of arcsec and sub-arcsec which makes the demanding for observation instruments are higher and higher. For solar telescope, the atmospheric interference, the orbital precession and the attitude changes of spacecraft [1] and the revolving of the moving parts will all cause the random vibration of the platform [2,3] and also it will affect the high imaging precision due to blurring images. Therefore it is very necessary to take measures to suppress vibration of the platform of spacecraft or realizing solar magnetic field images registration [4,5] at EUV wavelengths to obtain solar magnetic image with high spatial resolution and high precision displacement analysis [6].

*Corresponding author: Yang Liu, Changchun Institute of Optics, Fine Mechanics and Physics, Chinese Academy of Sciences, Changchun, Jilin 130033, China. E-mail: liuy_ciomp@163.com.

The solar optical telescope onboard SOLAR-B [7] and ANGARA on the big solar vacuum telescope [8] all use solar granulation to calculate the displacement which solar images are visible wavelength (629–634 nm) with correlation tracker. Advantages of calculating the displacement using solar granulation images in visible wavelength are that optical systems in visible wavelength are easy to design, including detectors and optical lenses. Solar granulation changes slowly compared to solar magnetic field images in EUV wavelengths for solar activities such as solar prominence, solar flares, solar corona and sunspot, so it's relatively easy to use solar granulation images in visible wavelength to calculate the displacement, Shortcomings of calculating the displacement using solar granulation images in visible wavelength are structural complexity that complicated correlation tracker is normally adopted. Comparing to adaptive optical systems that image stabilizers are simpler and less expensive, so using image stabilizers is especially rewarding. However, the researches of the quality on solar images for calculating displacements by DIC are very few, and there are many studies on these researches in mechanical and material fields.

Because of the association with uniqueness, the accuracy of correlation measurement is seriously affected by the quality of speckle pattern. Therefore undoubtedly, speckle pattern assessment to the users of DIC is a crucial issue. Pan et al. who verified the correlation measurement accuracy of different speckle patterns [9], and presented a replaceable method that the average pattern gradient has a certain relationship with the relative measurement accuracy [10]. Yuan et al. [11] had studied the close relationship between the size of subset and speckle size and the measurement accuracy. In consideration of the small regional fluctuation of speckle, mean subset fluctuation [12], subset entropy [13] and Shannon entropy [22] were presented.

A local parameter which is employed to assess the quality of solar magnetic field images at EUV wavelengths called comprehensive consideration of mean subset intensity and gradients (CCMSIG) is presented in this paper. Firstly, it briefly explains the DIC principle based on nonlinear gradient iterative algorithm. Secondly, the formula of qualitative CCMSIG of the solar magnetic field images at EUV wavelengths is presented; Followed by it is the discussion on the CCMSIG values of active region, flare region, and coronal hole images. At last, in order to verify the effectiveness of CCMSIG in assessing the quality of the solar magnetic field images at EUV wavelength, lots of experiments are performed. The results show that the relationship between the displacement measurements errors and CCMSIG are very close. Accuracy of displacement measurement in DIC was greatly raised by regional images with smaller CCMSIG.

2. Principle of digital image correlation method

2.1. Nonlinear gradient iterative algorithm

Due to the solar magnetic field evolution and the rapid changing in the solar active area and the offset and gain variation of imaging device and non-uniform sensor pixels in the deformed images, so a more accurate intensity variation mathematical model could be adopted in order to minimize the measurement error. Therefore, a non-linear intensity variation model is used to express the connection of the intensity value of a physical point between the reference part area and the homologous point in the deformed part area [14]. Figure 1 shows the model which takes the above factors into account [15].

$$\varphi\left(x_j', y_j'\right) = a \times \beta^3\left(x_j, y_j\right) + b \times \beta\left(x_j, y_j\right) + c,\ j = 1, 2, \ldots, j_0 \tag{1}$$

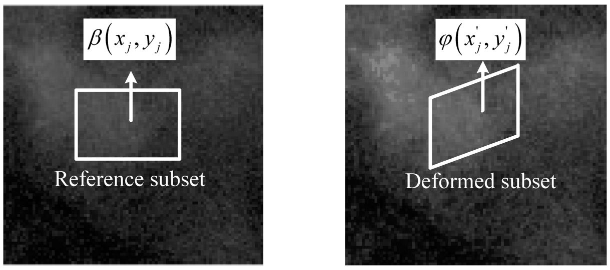

Fig. 1. Intensity variation model of solar magnetic field images at EUV wavelength with the point in the reference part 91 $\times$ 91 pixels and deformed part 91 $\times$ 91 pixels.

Where $\beta(x_j, y_j)$ is the gray intensity value at the point (x_j, y_j) of the reference part image, $\varphi(x_j', y_j')$ is the gray intensity at the homologous point (x_j', y_j') of the deformed part region, b and a are the linear and cubic factors of the intensity changes, respectively, and c presents the offset of the intensity changes.

The solar image is deformed because of the solar magnetic field varies continuously. Therefore, a square subset is selected around point (x_c, y_c) whose deformed displacement values are the issues we need to analyze [16,17]. The subset in the changed image does not change if the subset is small enough, so the first-order shape function coordinates of the points (x_j', y_j') of the changed part region mapped to the points (x_j, y_j) around the part center (x_c, y_c) in the subset of reference could be indicated as:

$$x_j' = x_j + \Delta\sigma + \sigma_x'\Delta x_j + \sigma_y'\Delta y_j \tag{2}$$

$$y_j' = y_j + \Delta\tau + \tau_x'\Delta x_j + \tau_y'\Delta y_j \tag{3}$$

Where $\Delta\sigma$ and $\Delta\tau$ are the sub-pixel shift parameters of the reference part center in orthorhombic directions, respectively; σ_{jx}', σ_{jy}', τ_{jx}' and τ_{jy}' are the deformation of the reference part center; Δx_j and Δy_j are the difference values from (x_j, y_j) to the subset center (x_c, y_c), $\Delta x_j = x_j - x_c$, $\Delta y_j = y_j - y_c$. Substituting Eqs (2) and (3) into Eq. (1), the expression of the intensity at the point (x_j', y_j') in the deformed part region and its homologous point (x_j, y_j) of the part of reference image could be showed as:

$$Q_j\left(\vec{P}\right) = \varphi\left(x_j', y_j'\right) - a \times \beta^3\left(x_j, y_j\right) - b \times \beta\left(x_j, y_j\right) - c \cong 0 \tag{4}$$

Where $\vec{P} = [\Delta\sigma, \sigma_x', \sigma_y', \Delta\tau, \tau_x', \tau_y', a, b, c]^T$ is the quested argument vector which includes sub-pixel displacement gradients and displacements of the part, that is the requested argument vector, and σ_x', σ_y', τ_x', τ_y', which are sub-pixel displacement gradients, are actually much less than $\Delta\sigma$, $\Delta\tau$, which are the sub-pixel shift parameters of the reference part center in orthorhombic directions respectively, so the initial value of σ_x', σ_y', τ_x', τ_y' are generally set to zero, b and a are the linear and cubic factors of the intensity changes, respectively, and c presents the offset of the intensity changes. In a short exposure time, solar magnetic field evolution is mostly linear, so the initial value of a, c are generally set to zero, the linear b factor of the intensity changes converges around 1 according to multiple simulation verification. $\Delta\sigma$ and $\Delta\tau$ are the sub-pixel shift parameters of the reference part center in orthorhombic directions, respectively.

The above Eq. (4) $\vec{Q}(\vec{P}^k)$ could be solved by iteration method [19]:

$$\vec{Q}\left(\vec{P}^k\right) + \nabla\vec{Q}\left(\vec{P}^k\right)\left(\vec{P}^{k+1} - \vec{P}^k\right) = 0 \tag{5}$$

Where $\vec{P}^k$ and $\vec{P}^{k+1}$ are the solutions in the iterative process, respectively.

$$\nabla Q_j\left(\vec{P}\right) = \left[\varphi_{jx}', \varphi_{jx}'\Delta x_j, \varphi_{jx}'\Delta y_j, \varphi_{jy}', \varphi_{jy}'\Delta x_j, \varphi_{jy}'\Delta y_j, -\beta_j^3, -\beta_j, -1\right] \tag{6}$$

Where φ'_{jx} and φ'_{jy} are the orthorhombic directional spatial gradient values of the deformed subset of the point (x'_j, y'_j), respectively. Because the iterative points may be not at internal-pixel position during iterative process, in this paper, gray $\varphi(x'_j, y'_j)$ is calculated by adopting the bilinear interpolation algorithm, and the gradients φ'_{jx}, φ'_{jy} can be implemented with Barron operator:

$$\begin{aligned}\varphi'_{jx}\left(x'_j(k), y'_j(k)\right) = \frac{1}{12}\varphi\left(x'_j(k)-2, y'_j(k)\right) - \frac{8}{12}\varphi\left(x'_j(k)-1, y'_j(k)\right) \\ +\frac{8}{12}\varphi\left(x'_j(k)+1, y'_j(k)\right) - \frac{1}{12}\varphi\left(x'_j(k)+2, y'_j(k)\right)\end{aligned} \tag{7}$$

$$\begin{aligned}\varphi'_{jy}\left(x'_j(k), y'_j(k)\right) = \frac{1}{12}\varphi\left(x'_j(k), y'_j(k)-2\right) - \frac{8}{12}\varphi\left(x'_j(k), y'_j(k)-1\right) \\ +\frac{8}{12}\varphi\left(x'_j(k), y'_j(k)+1\right) - \frac{1}{12}\varphi\left(x'_j(k), y'_j(k)+2\right)\end{aligned} \tag{8}$$

For the $j = 1, 2, \ldots, j_0 (j_0 > 9)$ points, the solution of Eq. (5) can be acquired by the iterative least squares method:

$$\vec{Q}\left(\vec{P}^{k+1}\right) = \vec{Q}\left(\vec{P}^{k}\right) + \nabla\vec{Q}\left(\vec{P}^{k}\right)\left(\vec{P}^{k+1} - \vec{P}^{k}\right) = \vec{Q}\left(\vec{P}^{k}\right) + \nabla\vec{Q}\left(\vec{P}^{k}\right)\left(\Delta\vec{P}^{k}\right) = \vec{0} \tag{9}$$

$$\vec{Q}\left(\vec{P}^{k}\right) = -\nabla\vec{Q}\left(\vec{P}^{k}\right)\left(\Delta\vec{P}^{k}\right) \tag{10}$$

The convergence condition of the iterative procedure is repeated until the calculation tolerance $\|(\Delta\vec{P}^k)\|$ is small enough or reaches the maximum number of iterations.

2.2. *Quality evaluation of solar magnetic field image sat EUV wavelength*

Substituting Eqs (2) and (3) into Eq. (4), ignoring the higher terms, the first order Taylor expansion of $Q_j(\vec{P})$ at (x'_j, y'_j) is:

$$\begin{aligned}Q_j\left(\vec{P}\right) = \varphi_j + \left[\Delta\sigma + \sigma'_x\Delta x_j + \sigma'_y\Delta y_j\right]\varphi'_{jx} + \left[\Delta\tau + \tau'_x\Delta x_j + \tau'_y\Delta y_j\right]\varphi'_{jy} \\ -a\times\beta_j^3 - b\times\beta_j - c \cong 0\end{aligned} \tag{11}$$

Operate norm to Eq. (11):

$$\left\|\vec{Q}\left(\vec{P}^{k}\right)\right\| = \left\|\nabla\vec{Q}\left(\vec{P}^{k}\right)\left(\Delta\vec{P}^{k}\right)\right\| \leqslant \left\|\nabla\vec{Q}\left(\vec{P}^{k}\right)\right\|\left\|\left(\Delta\vec{P}^{k}\right)\right\| \tag{12}$$

In this paper, take 2 norms, then substituting Eqs (6) and (11) into Eq. (12):

$$\left\|\left(\Delta\vec{P}^{k}\right)\right\|_\infty \geqslant \frac{\left\|\vec{Q}\left(\vec{P}^{k}\right)\right\|_\infty}{\left\|\nabla\vec{Q}\left(\vec{P}^{k}\right)\right\|_\infty} = \tag{13}$$

$$\frac{\max\left|\varphi_j + \left[\Delta\sigma + \sigma'_x\Delta x_j + \sigma'_y\Delta y_j\right]\varphi'_{jx} + \left[\Delta\tau + \tau'_x\Delta x_j + \tau'_y\Delta y_j\right]\varphi'_{jy} - a\times\beta_j^3 - b\times\beta_j - c\right|}{\max\left(\left|\varphi'_{jx}\right| + \left|\varphi'_{jx}\Delta x_j\right| + \left|\varphi'_{jx}\Delta y_j\right| + \left|\varphi'_{jy}\right| + \left|\varphi'_{jy}\Delta x_j\right| + \left|\varphi'_{jy}\Delta y_j\right| + \left|\beta_j^3\right| + |\beta_j| + 1\right)}$$

When we expand the absolute value of the numerator of Eq. (13), we get:

$$\frac{\begin{gathered}\max\left[|\varphi_j| + \left|\Delta\sigma + \sigma'_x\Delta x_j + \sigma'_y\Delta y_j\right|\left|\varphi'_{jx}\right| + \left|\left(\Delta\tau + \tau'_x\Delta x_j + \tau'_y\Delta y_j\right)\right|\left|\varphi'_{jy}\right| + \right. \\ \left.\left|a\times\beta_j^3 + b\times\beta_j + c\right|\right]\end{gathered}}{\max\left(\left|\varphi'_{jx}\right| + \left|\varphi'_{jx}\Delta x_j\right| + \left|\varphi'_{jx}\Delta y_j\right| + \left|\varphi'_{jy}\right| + \left|\varphi'_{jy}\Delta x_j\right| + \left|\varphi'_{jy}\Delta y_j\right| + \left|\beta_j^3\right| + |\beta_j| + 1\right)} \tag{14}$$

The x-coordinate difference Δx_j and y-coordinate difference Δy_j between point (x'_j, y'_j) and center point (x'_c, y'_c) are approximately set as the maximum value $N/2$, Eq. (12) can be approximated as:

$$\frac{\max\left[|\varphi_j| + \left|\Delta\sigma + \frac{N}{2}\left(\sigma'_x + \sigma'_y\right)\right|\left|\varphi'_{jx}\right| + \left|\left(\Delta\tau + \frac{N}{2}\left(\tau'_x + \tau'_y\right)\right)\right|\left|\varphi'_{jy}\right| + \left|a \times \beta_j^3 + b \times \beta_j + c\right|\right]}{\max\left((1+N)\left(\left|\varphi'_{jx}\right| + \left|\varphi'_{jy}\right|\right) + \left|\beta_j^3\right| + |\beta_j| + 1\right)} \tag{15}$$

Then, approximate the deformation amount of point (x'_j, y'_j) in the horizontal and vertical directions, σ'_{jx}, σ'_{jy}, τ'_{jx} and τ'_{jy}, to a pixel value, Eq. (15) can be approximated as:

$$\frac{\max\left[|\varphi_j| + (1+N)\left(\left|\varphi'_{jx}\right| + \left|\varphi'_{jy}\right|\right) + \left|a \times \beta_j^3 + b \times \beta_j + c\right|\right]}{\max\left((1+N)\left(\left|\varphi'_{jx}\right| + \left|\varphi'_{jy}\right|\right) + \left|\beta_j^3\right| + |\beta_j| + 1\right)} \tag{16}$$

When the deformation amount of the subset image is not too large, the gray values of the corresponding points (x'_j, y'_j) and (x_j, y_j) in the distorted subset image and the reference subset image can be approximately considered to be equal, that is, $\varphi_j \cong \beta_j$, meanwhile, the gray gradients of point d (x_j, y_j) in the horizontal and vertical directions can be approximately considered to be equal, that is, $\varphi'_{jx} \cong \beta'_{jx}$, $\varphi'_{jy} \cong \beta'_{jy}$, then Eq. (16) can be approximately expressed as:

$$\frac{\left[|\beta_j| + (1+N)\left(\left|\beta'_{jx}\right| + \left|\beta'_{jy}\right|\right) + \left|a \times \beta_j^3 + b \times \beta_j + c\right|\right]}{\left((1+N)\left(\left|\beta'_{jx}\right| + \left|\beta'_{jy}\right|\right) + \left|\beta_j^3\right| + |\beta_j| + 1\right)} \tag{17}$$

After sorting out, the following formula is obtained:

$$\left\|\left(\Delta\vec{P}^k\right)\right\|_\infty \cong \frac{(1-|a|)\left|\beta_j^3\right| - |b| \times |\beta_j| + 1 - c}{(1+N)\left(\left|\beta'_{jx}\right| + \left|\beta'_{jy}\right|\right) + \left|\beta_j^3\right| + |\beta_j| + 1} \tag{18}$$

Further, the gray value β_j at point (x_j, y_j) is approximately expressed as the average gray value $\overline{\beta}$ of the image subset, the approximate sum of horizontal gray gradient β'_{jx} and vertical gray gradient β'_{jy} is the average gray gradient value $\overline{\beta}'$ of the entire image subset, and the formula follows:

$$\left\|\left(\Delta\vec{P}^k\right)\right\|_\infty \cong \frac{(1-|a|)\left|\overline{\beta}^3\right| - |b| \times \left|\overline{\beta}\right| + 1 - c}{(1+N)\left|\overline{\beta}'\right| + \left|\overline{\beta}^3\right| + \left|\overline{\beta}\right| + 1} \tag{19}$$

From Eq. (19) we can see, it is a good way to find a parameter comprehensive consideration of mean subset intensity and gradients (CCMSIG) to define the local image quality, and based on the CCMSIG measurement accuracy of the displacement of DIC could be predicted quantitatively. It is feasible to evaluate the effect of each subset on image quality by its displacement measurement, and the displacement measurement accuracy gets higher with the subset images smaller CCMSIG.

3. Numerical experiments

3.1. Regional samples of solar magnetic field images at EUV wavelength

In this paper, numerical simulated experiments are conducted, due to their easily controlled features, which verify that the CCMSIG is a novel parameter for the quality assessment of regional samples of

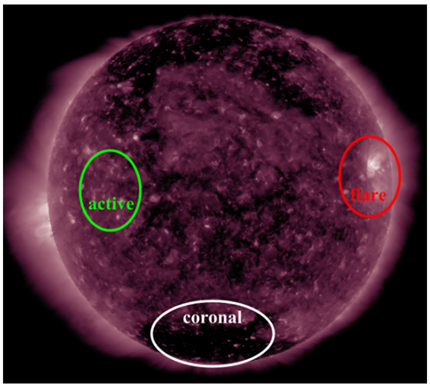

Fig. 2. Solar magnetic field images at EUV wavelength 211 Å.

solar magnetic field images at EUV wavelength 211 Å with DIC method. The experimental method eliminates the possible errors causing by solar magnetic evolution, satellite attitude changes and random satellite jitter.

Figure 2 shows solar magnetic field images of space solar telescope at wavelength 211 Å obtained from SDO AIA (Atmospheric Imaging Assembly). These images take series remote sensing images of the solar atmosphere through multi-band with 8-bit with dimensions of 4096 × 4096 pixels.

Active region, flare region, and coronal hole calculated in the numerical researches with their histograms are illustrated in Fig. 3. Figure 2 is taking the three 8-bit (0 to 255 gray scale) regions with a resolution with 600 × 200 pixels. In Fig. 3 we can see that there are huge differences among grayscale distributions of the three regional images. Using Eq. (19) we could calculate the CCMSIG values with subset size in the three regions at regularly distributed points (15 × 51 with a distance of 10 pixels) [18,19]. Table 1 shows the results from which we could see the CCMSIG of active region is about 0.2 times of the CCMSIG of flare region while the CCMSIG of active region is about 0.004 times of the CCMSIG of coronal hole.

3.2. *Mean bias error and STD for displacement measurement*

In order to quantitatively assess the accuracy of the digital image correlation for calculating displacements, the calculated displacements errors are divided: mean bias error and STD for displacement measurement. The mean bias error of the calculated results can be showed as:

$$b_{error} = b_{mean} - b_{imposed} \tag{20}$$

Where $b_{mean} = (1/j_0)\sum_{j=1}^{j_0} b_j$ indicates the average of the j_0 calculated displacement errors and $b_{imposed}$ represents the displacement generated by simulation.

The STD of the calculated results can be showed as:

$$\sigma_{error} = \sqrt{\left({}^{1}\!/_{(j_0 - 1)}\right)\sum_{j=1}^{j_0}(b_j - b_{mean})} \tag{21}$$

Table 1
CCMSIG of 211 Å, 131 Å and 94 Å solar EUV images used in numerical experiment

Band (Å)	Subset size (pixels)	17 × 17	23 × 23	29 × 29	35 × 35	41 × 41	47 × 47	53 × 53	59 × 59	65 × 65	71 × 71	77 × 77	83 × 83
211	Active region ($\times 10^{-3}$)	5.03	4.75	4.46	4.17	3.88	3.58	3.27	2.97	2.65	2.33	2.02	1.68
	Flare region ($\times 10^{-2}$)	3.62	3.24	2.98	2.64	2.37	2.03	1.75	1.42	1.28	0.93	0.67	0.34
	Coronal hole ($\times 10^{-1}$)	8.57	8.66	8.75	8.78	8.80	8.75	8.63	8.47	8.23	7.92	7.52	6.99
131	Active region ($\times 10^{-3}$)	1.57	1.47	1.38	1.28	1.18	1.09	0.994	0.896	0.799	0.696	0.597	0.491
	Flare region ($\times 10^{-3}$)	2.37	2.29	2.21	2.11	2.00	1.89	1.76	1.62	1.48	1.32	1.16	0.993
94	Active region ($\times 10^{-3}$)	2.73	2.55	2.37	2.19	2.01	1.82	1.64	1.46	1.27	1.08	0.894	0.703
	Flare region ($\times 10^{-3}$)	6.04	5.77	5.48	5.18	4.85	4.51	4.15	3.77	3.38	2.95	2.51	2.04

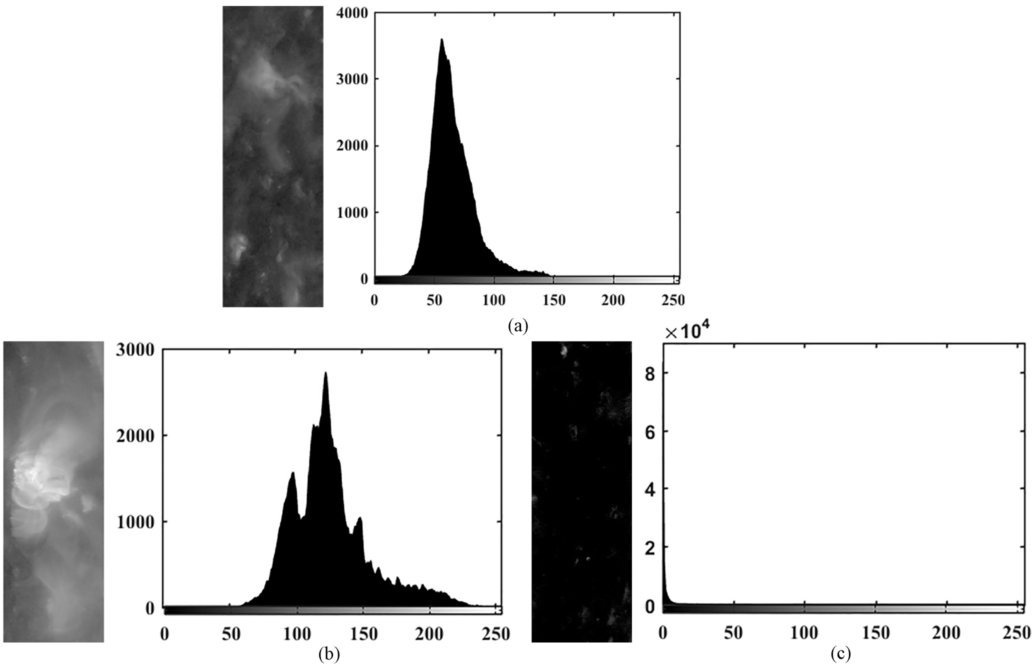

Fig. 3. Regional samples of solar magnetic field images at EUV wavelength 211 Å: (a) active region and its histogram, (b) flare region and its histogram, (c) coronal hole and its histogram.

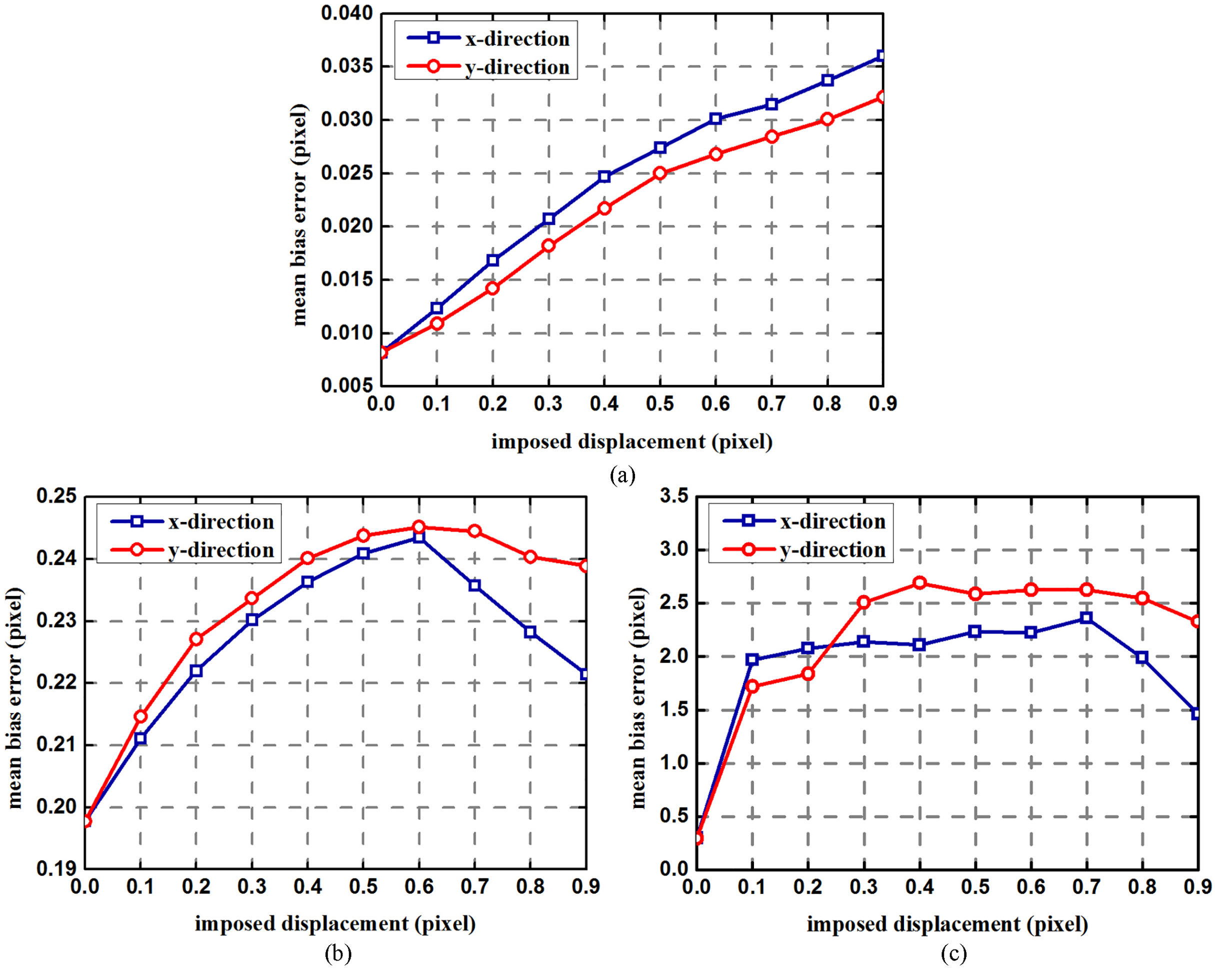

Fig. 4. Mean bias error of calculated displacement sin the x and y directions as a function of sub-pixel displacement for the three regional images by 41× 41 pixels part: (a) active region, (b) flare region, (c) coronal hole.

4. Results

4.1. Mean bias error and STD by sub-pixel displacement

As Fig. 3 shown, a large number of translations are applied to the three regional images, and the range is from 0.1 to 0.9 pixels by a pace of 0.1 pixels in both y direction and x direction, and a range of translated images are generated. At regularly distributed points (15 × 51 with a distance of 10 pixels), using nonlinear gradient iterative algorithm, the displacement errors between the original subsets and the translated subsets are calculated.

In reference of [14], the non-linear intensity change model is adopted to calculate whole field displacement and strain measurement. In references of [15], solar activities such as solar prominence, solar flares, solar corona and sunspots are mainly shown in short wave EUV and X ray bands, and the deformed images at different time usually exists the solar magnetic field evolution and the rapid change in the solar active area and the offset and gain variation of imaging device, non-uniform sensor pixels,

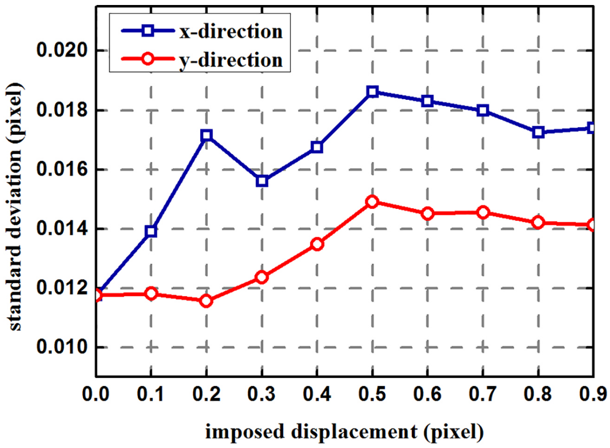

(a)

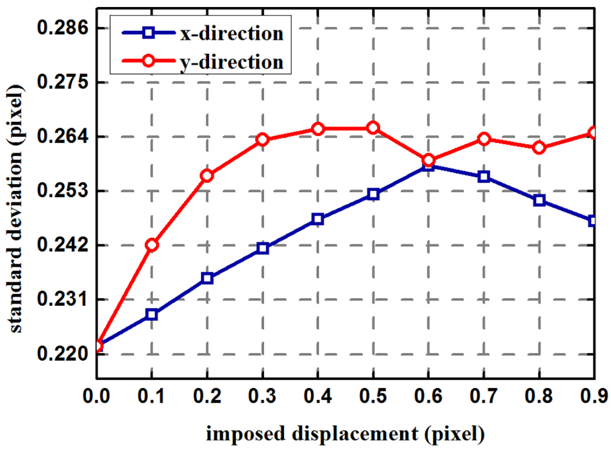

(b)

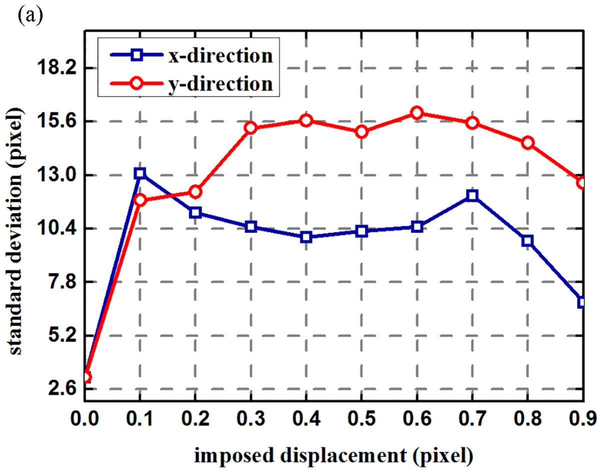

(c)

Fig. 5. STD of calculated displacements in the x and y directions as a function of sub-pixel displacement for the three regional images by 41 × 41 pixels part: (a) active region, (b) flare region, (c) coronal hole.

and also satellite attitude changes during solar magnetic field images acquisition, so the connection of the intensity value of a physical point between the reference part region and the homologous point in the deformed part region can be expressed as that the shifted images are adjusted further artificially with brightness increased by 10%. Afterwards, images are handled to imitate true solar magnetic activation in EUV waveband using the following mapping function:

$$Q_{out} = \begin{cases} 1.2 \times Q_{in}\ if\ Q_{in} \geqslant 0.9Q_{in\_max} \\ 1.1 \times Q_{in}\ if\ 0.8Q_{in\_max} \leqslant Q_{in} < 0.9Q_{in\_max} \\ Q_{in} \qquad if\ Q_{in} < 0.8QI_{in\_max} \end{cases} \tag{22}$$

Where Q_{out} and Q_{in} are on behalf of the solar field images which are after and before handling, and Q_{in_max}. is the maximum gray value of each image.

The mean bias errors of calculated displacements as a function of imposed sub-pixel shift values for the three regional images using 41 × 41 pixels part are shown Fig. 4. Figure 4 shows some very important consequences: (1) Basically, the mean bias error is increasing with the increasing of sub-pixel displacement; (2) The mean bias errors of the three regional images are different. As shown in Fig. 4, it is

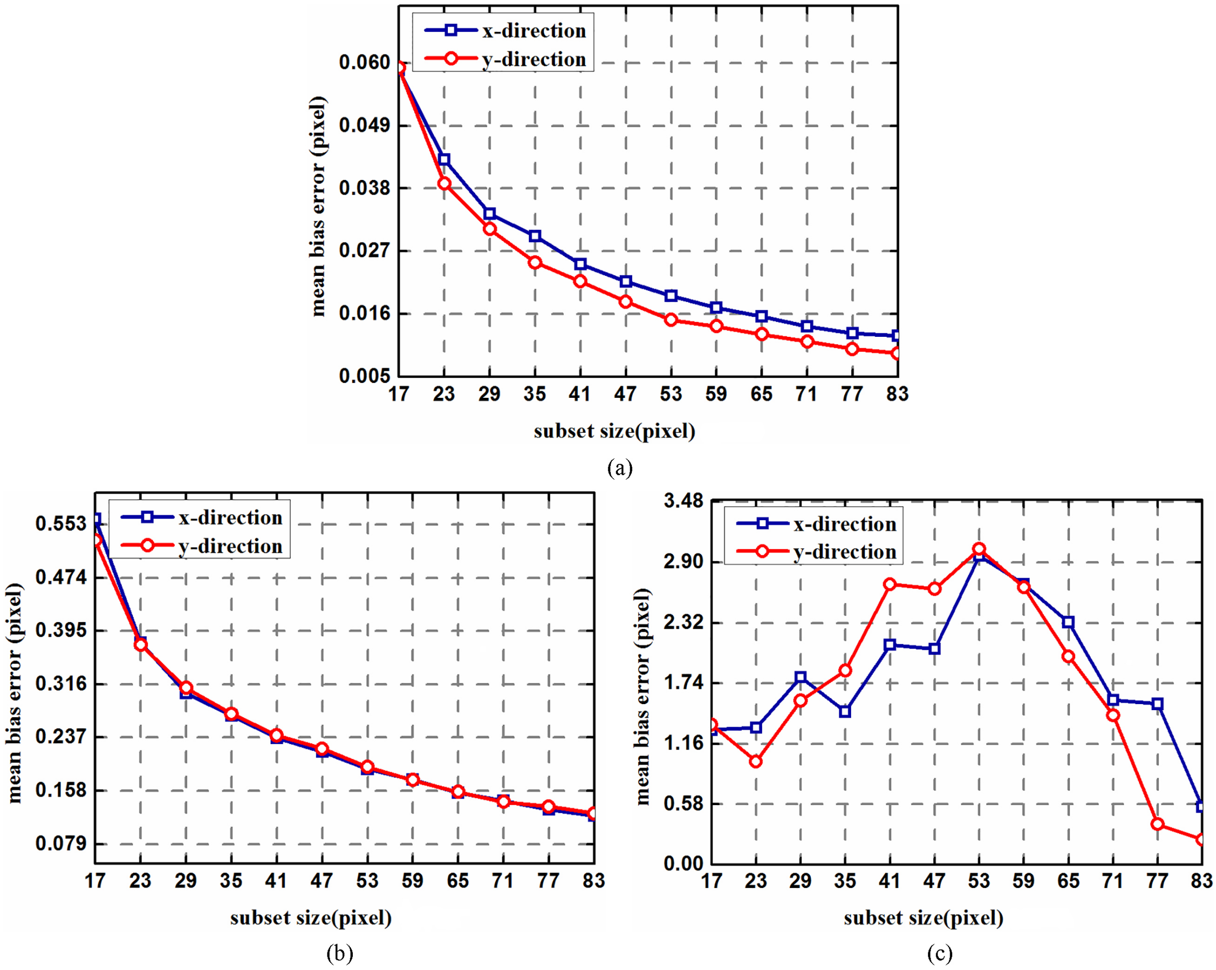

Fig. 6. Mean bias error of calculated displacements in the x and y directions by 0.4 pixel as a function of local image sizes for the three regional images: (a) active region, (b) flare region, (c) coronal hole.

obviously that the active region with smaller CCMSIG produces smaller mean bias error, and the coronal hole with larger CCMSIG produces larger mean bias error; (3) The relative values of mean bias error in the three regions are very close to Eq. (19).The observation results fit theoretical prediction perfectly. The consequences above obviously show that, to assess the mean bias error of the regional images of solar magnetic field images at EUV wavelength 211 Å for calculating displacements, CCMSIG is very an effective parameter.

The STD of calculated displacement for the three regional images by 41 $\times$ 41 pixels part are shown in Fig. 5. From Fig. 5 we could see that: (1) Basically, the standard deviation errors are increasing with the increasing of sub-pixel displacement; (2) The active region with smaller CCMSIG generates smaller standard deviation error; (3) The relative values of mean bias error in the three regions quite accord with Eq. (19).Theoretical model of Eq. (19) can well explain these three consequences,which further shows that for estimating regional images of solar magnetic field images at EUV wavelength 211 Å for calculating displacements, CCMSIG can be used as an effective parameter.

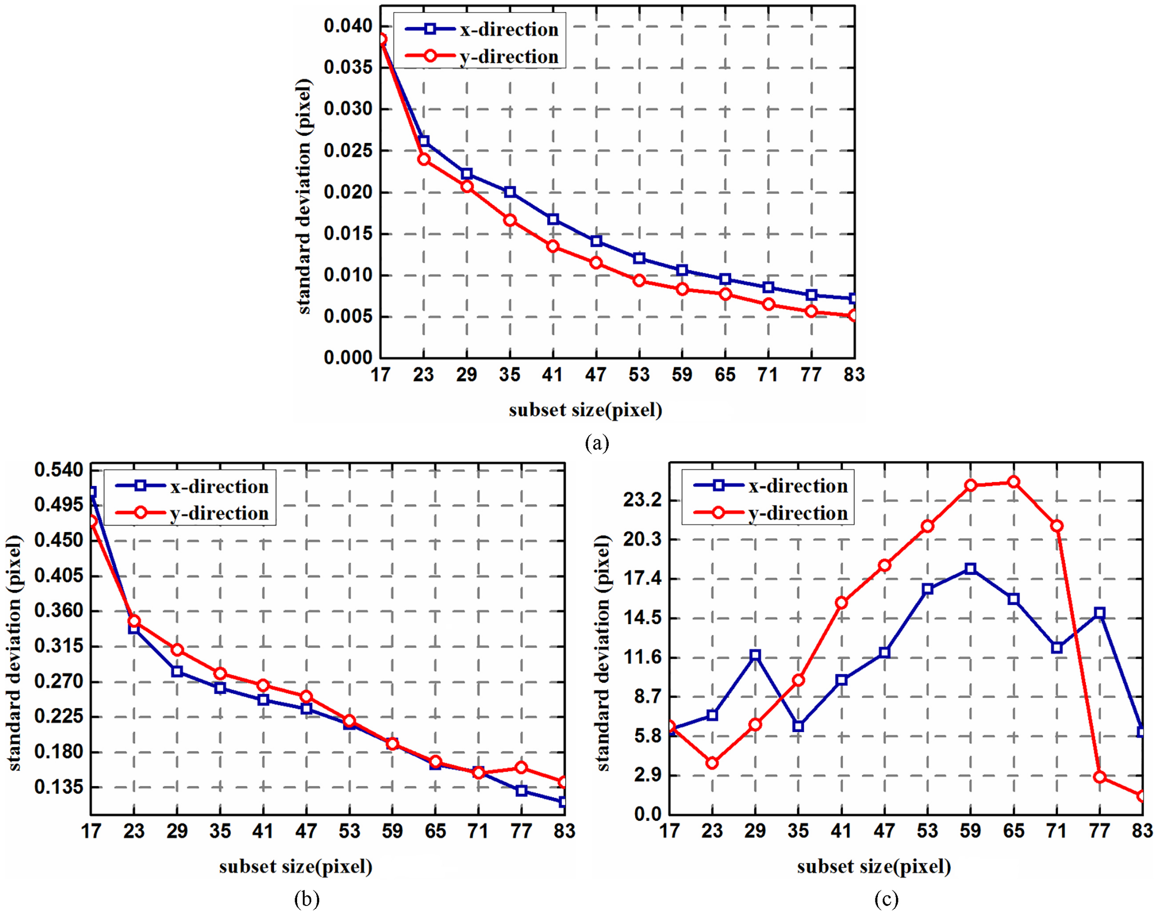

Fig. 7. STD of calculated displacements in the x and y directions by 0.4 pixel as a function of local image sizes for the three regional images: (a) active region, (b) flare region, (c) coronal hole.

4.2. *Effect of regional image size on sub-pixel displacement calculation*

The correctness of the theoretical model is further proved by calculating the sub-pixel translated images with 0.4 pixels of the three regional images in which local image sizes ranges from 17×17 to 83×83 pixels increased by 6 pixels [20,21]. As shown in Figs 6 and 7, it is obviously that mean bias errors and STD decrease as the local size increasing for these three computed image pairs. It is known from Eq. (19), that the local image is a larger one, the displacement measurement accuracy could be improved due to the decrease of CCMSIG.

It can be very clearly seen that the mean bias error and STD are different for the three regional images even if the identical local image is calculated in the DIC computations. Citing an instance, the mean bias error and STD of the displacements calculated from active region are quite smaller compared to those obtained from flare region and coronal hole, which could be well explained by the fact that the mean bias error and STD produced by active region with minimum CCMSIG are the smallest, and the largest the mean bias error and STD are always yield by coronal hole with maximum CCMSIG. The relative values of mean bias error and STD in the three regions are a lot closer to Table 1.

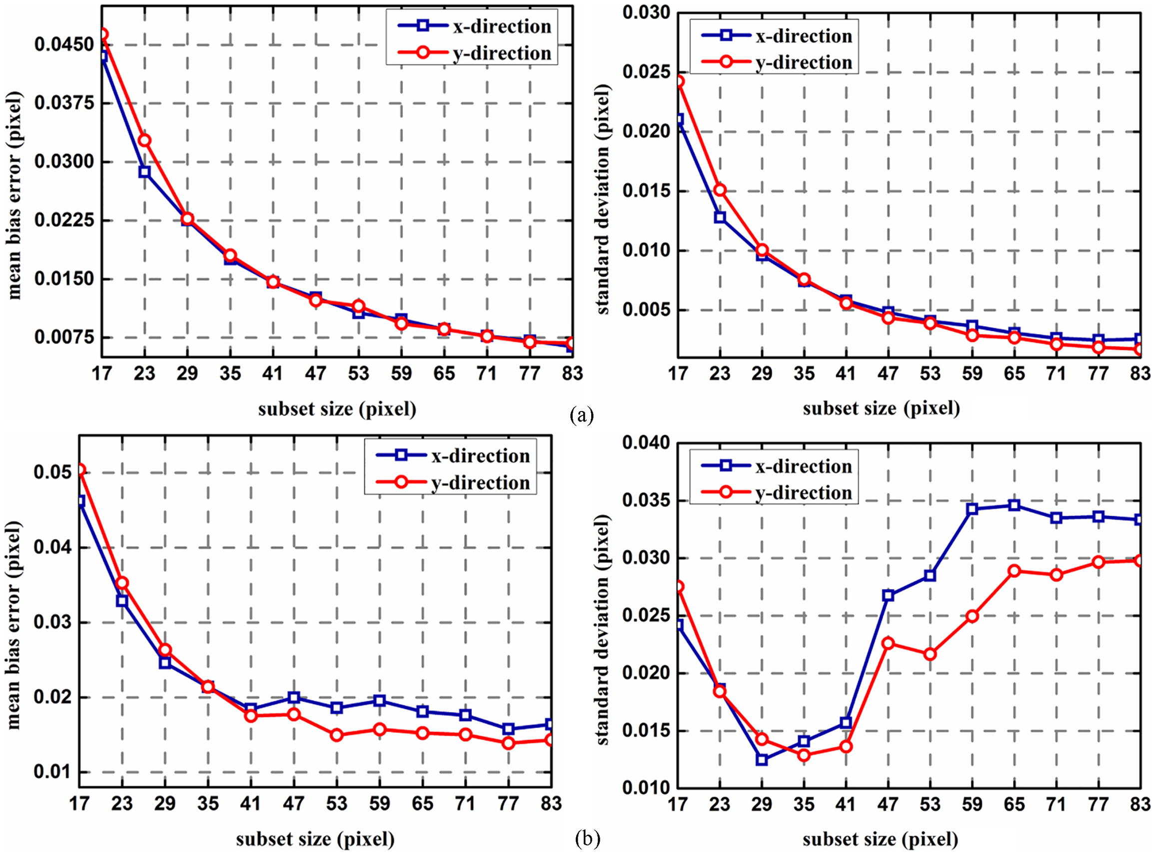

Fig. 8. Mean bias error and STD of calculated displacements in the x and y directions by 0.4 pixel as a function of local image sizes for the two regional images: (a) active region, (b) flare region in 94 Å wavelength.

For the reason above, the consequences are quite reasonable shown in Figs 6 and 7. Just as it is expected, the mean bias error and STD, and the prediction calculated by Eq. (19) are very consistent.

The correctness of the theoretical model is further proved by calculating the sub-pixel translated images with 0.4 pixels of the 94 Å and 131 Å solar EUV regional images in which local image sizes ranges from 17×17 to 83×83 pixels increased by 6 pixel. As shown in Figs 6 and 7. It is obviously that mean bias errors and STD decrease as the local size increasing for these computed image pairs, and coronal holes in 94 Å and 131 Å solar EUV images are very small, so this paper does not carry out calculation.

5. Discussion

In the previous sections, through predicting the displacement measurement precision, we prove the effectiveness of CCMSIG, and as we all know that the accuracy of displacement measurement is affected greatly by the subset size.

The experimental results are in according with the theoretical analysis (Eq. (19)) on which the subset images with smaller CCMSIG could lead to higher displacement measurement accuracy, and the measurement accuracy is quite improved by using larger local image. However, along with further the increasing of a local image size, the increasing of measurement accuracy are quiet slowly. For the other

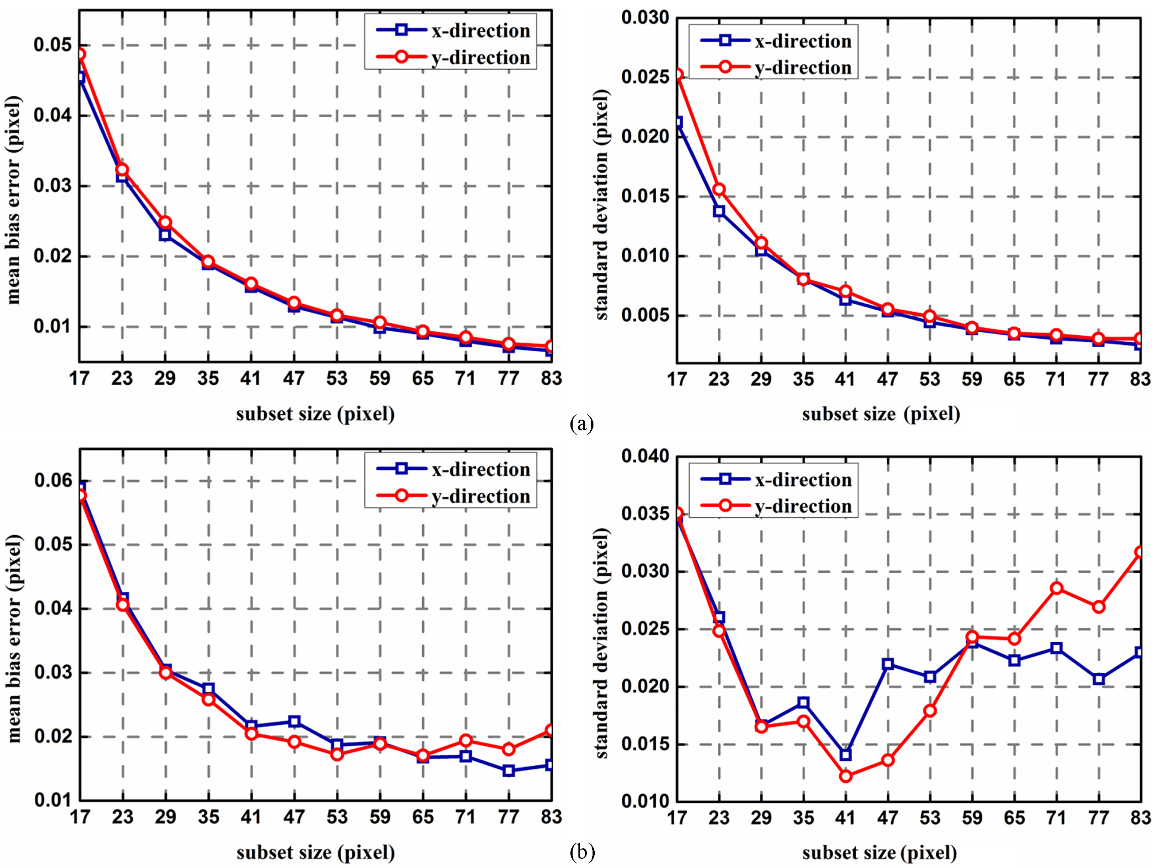

Fig. 9. Mean bias error and STD of calculated displacements in the x and y directions by 0.4 pixel as a function of local image sizes for the two regional images: (a) active region, (b) flare region in 131 Å wavelength.

side, in measured displacements, supererogatory systematic errors will be produced by a too larger local image size.

6. Conclusion

Comprehensive consideration of mean subset intensity and gradients(CCMSIG), which is a simple but effective local parameter, is presented by this paper to evaluate the quality of the regional subset images for solar magnetic field images at EUV wavelengths used in DIC. Through a large number of experiments using the three regional images (active region, flare region, and coronal hole), the effectiveness and correctness of this novel concept is proved. From the experimental result we can see that both mean bias errors and STD of the measured displacement are quite in connection with the CCMSIG of the regional images, and that the subsets with smaller CCMSIG generates the smaller mean bias error and STD. As well, we can see from the present research that this new parameter for the regional subset images quality evaluation of solar magnetic field images at EUV wavelengths could be applied as instructions for practical region choice for different needs of the displacement measurement accuracy.

This algorithm is mainly applied in two aspects, on the one hand, the continuous solar EUV images collected by the space solar imager are accurately matched on the ground to enhance the signal-to-noise ratio of the images, so that the image resolution is higher. This application does not require high real-time computing, and this algorithm is very suitable. On the other hand, the sun image displacement caused by the satellite itself and solar evolution is detected in real time by the solar images on space solar telescope, but this application of the algorithm requires some preconditions. High speed hardware calculation unit is required to ensure fast calculation of iteration process, and the algorithm needs to be simplified according to practical application, and the darker EUV signal is enhanced to allow rapid imaging by image intensifier.

Acknowledgments

This work is supported by the Strategic Priority Research Program of Chinese Academy of Science (CAS). Grant No.XDA15320103.

References

[1] D. Inamdar, G. Leblanc and R.J. Soffer, The correlation coefficient as a simple tool for the localization of errors in spectroscopic imaging data, *Remote Sens* **10** (2018), 231.
[2] P. Hajireza, W. Shi, K. Bell and R.J. Paproski, Non-interferometric photo acoustic remote sensing microscopy, *LightSci Appl* **6** (2017), 16278.
[3] S.X. Ma and X. Guo, Frequency estimation of satellite-based automatic identification system signals, *J Comput. Methods Sci Eng* **16**(1) (2016), 29–37.
[4] X.F. Ou and P.C. Yan, Research of image impainting algorithm based on image segmentation, *J Comput Methods Sci Eng* **18**(3) (2018), 637–644.
[5] D.M. Wang and Y. Yang, A method based on an improved immune genetic algorithm for the feature fusion of the infrared and visible images, *J Comput Methods Sci Eng* **18**(3) (2018), 591–603.
[6] S. Jiang, X.B. Zhang, Y. Zhang and C.R. Hu, Subnanometer-resolved chemical imaging via multivariate analysis of tip-enhanced Raman maps, *LightSci Appl* **6** (2017), 17098.
[7] S. Toshifumi and E. Chris, Image stabilization system on SOLAR-B solar optical telescope. SPIE Astronomical Telescopes + Instrumentation, Glasgow, United Kingdom, 21–25 June 2004, John C. M., Proc. SPIE 5487 (2004).
[8] P.A. Konyaev, V.P. Lukin, O. Emallev and N.N. Botugina, Modified correlation tracker algorithm for tip-tilt correction system and project ANGARA on the Big Solar Vacuum Telescope. SPIE Astronomical Telescopes + Instrumentation, Orlando, Florida, United States, 24–31 May 2006, Brent L., Ellerbroek, Proc. SPIE 62725I (2006).
[9] Y.Q. Wang, M.A. Sutton and H.A. Bruck, Quantitative error assessment in pattern matching: effects of intensity pattern noise, interpolation, strain and image contrast on motion measurements, *Strain* **45** (2009), 160–178.
[10] B. Pan, Z.X. Lu and H.M. Xie, Mean intensity gradient An effective global parameter for quality assessment of the speckle patterns used in digital image correlation, *Opt Lasers Eng* **48** (2010), 469–477.
[11] Y. Yuan, Q. Zhan and J. Huang, Digital image correlation with gray gradient constraints: application to spatially variant speckle images, *Opt Lasers Eng* **77** (2016), 85–91.
[12] T. Hua, H.M. Xie and S. Wang, Evaluation of the quality of a speckle pattern in the digital image correlation method by mean subset fluctuation, *Optics & Laser Technology* **43** (2011), 9–13.
[13] Y.F. Sun and J.H.L. Pang, Study of optimal subset size in digital image correlation of speckle pattern images, *Opt Lasers Eng* **45** (2007), 967–974.
[14] X.Y. Liu, Q.C. Tan and L. Xiong, Performance of iterative gradient-based algorithms with different intensity change models in digital image correlation, *Optics Laser Technol* **44** (2012), 1060–1067.
[15] Y. Liu, K.F. Song and X.D. Wang, Displacement analysis of solar magnetic field images in EUV wavelengths of space solar telescope, *Int J of Pattern Recogn Artif Intel* **33** (2019), 1950005.
[16] P. Ferraiuoli, J.W. Fenner and A.J. Narracott, Analysis of speckle pattern quality and uncertainty for cardiac strain measurements using 3d digital image correlation, *Lecture Notes in Computational Vision and Biomechanics* **27** (2017), 883–892.
[17] J. Park, S. Yoon and T.H. Kwon, Assessment of speckle-pattern quality in digital image correlation based on gray intensity and speckle morphology, *Opt Laser Eng* **91** (2017), 62–72.
[18] P. Mazzoleni, E. Zappa and F. Matta, Thermo-mechanical toner transfer for high-quality digital image correlation speckle patterns, *Opt Lasers Eng* **75** (2015), 72–80.

[19] G. Crammond, S.W. Boyd and J.M. Barton, Speckle pattern quality assessment for digital image correlation, *Opt Lasers Eng* **51** (2013), 1368–1378.
[20] Z.Y. Wang, H.Q. Li and J.W. Tong, Statistical analysis of the effect of intensity pattern noise on the displacement measurement precision of digital image correlation using self-correlated images, *Exp Mech* **47** (2007), 701–707.
[21] B. Pan, H.M. Xie and Z.Y. Wang, Study on subset size selection in digital image correlation for speckle patterns, *Opt Express* **16** (2008), 737–748.
[22] X.Y. Liu, R.L. Li and H.W. Zhao, Quality assessment of speckle patterns for digital image correlation by Shannon entropy, *Optik* **126** (2015), 4206–4211.